Talanta 277 (2024) 126321

Contents lists available at ScienceDirect

Talanta

journal homepage: www.elsevier.com/locate/talanta

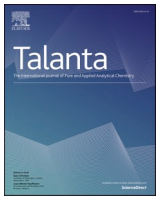

Electrochemiluminescence quenching effect of Cu_2O towards flower-like ferric ion-doped g-C_3N_4 and its application for Cyfra21-1 immunosensing

Hao Yu [a], Qianqian Cui [a], Fengdi Li [a], Yun Wang [a], Xianpeng Liao [a], Lihua Hu [a,*], Hongmin Ma [a], Dan Wu [a], Qin Wei [a,b,**], Huangxian Ju [a,c]

[a] Collaborative Innovation Center for Green Chemical Manufacturing and Accurate Detection, Key Laboratory of Interfacial Reaction & Sensing Analysis in Universities of Shandong, School of Chemistry and Chemical Engineering, University of Jinan, Jinan, 250022, PR China
[b] Department of Chemistry, Sungkyunkwan University, Suwon, 16419, Republic of Korea
[c] State Key Laboratory of Analytical Chemistry for Life Science, School of Chemistry and Chemical Engineering, Nanjing University, Nanjing, 210023, PR China

ARTICLE INFO

Keywords:
Electrochemiluminescence
Ferric ion-doped g-C_3N_4
Cuprous oxide nanocubes
Resonance energy transfer
Cyfra21-1

ABSTRACT

In this article, ferric ion-doped floral graphite carbon nitride (Fe–CN-3, energy donor) was used to construct the substrate of the immunosensor and copper oxide nanocubes (Cu_2O, energy acceptor) were taken as an efficient ECL quenching probe. A sandwich quench electrochemiluminescence (ECL) immunosensor for soluble cytokeratin 19 fragment (Cyfra21-1) detection was preliminarily developed based on a novel resonant energy transfer donor-acceptor pair. Fe–CN-3, a carbon nitride that combines the advantages of metal ion doping as well as morphology modulation, is used in ECL luminophores to provide more excellent ECL performance, which makes a significant contribution to the application and development of carbon nitride in the field of ECL biosensors. The regular shape, high specific surface area and excellent biocompatibility of the quencher Cu_2O nanocubes facilitate the labeling of secondary antibodies and the construction of sensors. Meanwhile, as an energy acceptor, the UV absorption spectrum of Cu_2O can overlap efficiently with the energy donor's ECL emission spectrum, making it prone to the occurrence of ECL-RET and thus obtaining an excellent quenching effect. These merits of the donor-acceptor pair enable the sensor to have a wide detection range of 0.00005–100 ng/mL and a low detection limit of 17.4 fg/mL (S/N = 3), which provides a new approach and theoretical basis for the clinical detection of lung cancer.

1. Introduction

As one of the worst cancers in the world, lung cancer has one of the highest rates of morbidity and death. Depending on the pathological form, it can be divided into two categories: small-cell lung cancer (SCLC) and non-small-cell lung cancer (NSCLC) [1]. Cytokeratin-19-fragment (Cyfra21-1) is a typical marker of NSCLC, and it is essential for the rapid identification and diagnostic identification of lung tumors. Its average content in humans should be less than 3.2 ng/mL. In consequence, the detection of Cyfra21-1 content can determine the survival status of lung cancer patients [2]. Numerous analytical techniques have been developed up to this point for Cyfra21-1 detection, including enzyme-linked immunosorbent assay (ELISA) [3], polymerase chain reaction (PCR) [4], immunoradiometric assay [5], surface plasmon resonance (SPR) [6], fluorescence immunoassay [7], inductively coupled plasma source mass spectrometry (ICP-MS) detection [8], and other methods. However, the practical application of these methods was limited due to several drawbacks, including complicated operation, long analysis time, low sensitivity, and a hefty cost. Hence, developing a sensitive technique to detect Cyfra21-1 is essential. Electrochemiluminescence immunoassays have gained popularity because of their wide detection range, short analysis time, low cost, and small number of samples required [9–11]. Herein, a sandwich electrochemical luminescence immunosensor with low background noise and high selectivity was constructed.

Resonance energy transfer (RET) is an electrodynamic phenomenon that uses long-range dipole-dipole interactions to generate nonradiative energy [12]. Besides, in the process of electrochemical luminescence

* Corresponding author.
** Corresponding author. Collaborative Innovation Center for Green Chemical Manufacturing and Accurate Detection, Key Laboratory of Interfacial Reaction & Sensing Analysis in Universities of Shandong, School of Chemistry and Chemical Engineering, University of Jinan, Jinan, 250022, PR China.
E-mail addresses: hulihua1206@163.com (L. Hu), sdjndxwq@163.com (Q. Wei).

https://doi.org/10.1016/j.talanta.2024.126321
Received 22 February 2024; Received in revised form 27 April 2024; Accepted 23 May 2024
Available online 27 May 2024

(ECL), species generated at electrodes undergo electron-transfer procedures to produce light-emitting excited states [13]. Further, electrochemiluminescence-resonance energy transfer (ECL-RET), an analytical method that combines all the advantages of both, has been increasingly used to analyze proteins, DNA, and micromolecules. Additionally, the ECL-RET system depends on a significant overlap between the energy acceptor's UV absorption spectrum and the energy donor's ECL emission spectrum [14]. The primary way the ECL-RET system works is that the acceptor can suppress the ECL emission from the donor, which manifests itself as a quenching probe of the ECL signal [15].

Graphitic carbon nitride (g-C_3N_4) finds extensive application in immunoassays and life medicine because of its excellent biocompatibility and electrochemical properties. g-C_3N_4 consists of large π-bond conjugated structures generated through sp^2 hybridization of N and C, which are called tri-*s*-triazine ring and triazine ring structure units [16]. These units extend indefinitely to form a network structure, and each network layer is connected by van der Waals force and hydrogen bonds [17]. So that it is the most stable allotrope among carbonaceous compounds [18]. However, due to g-C_3N_4's drawbacks, such as its slow charge transport, limited specific surface area, and quick charge recombination, its wide variety of applications is constrained [19,20]. Fortunately, several methods can be used to regulate the surface chemical properties of g-C_3N_4 at the molecular level, such as redox reactions, doping, and copolymerization due to its polymeric nature [21]. Among these methods, doping is a valuable technique to alter the electrical structure and energy band arrangement of the g-C_3N_4 material [22–25]. To be specific, doping of Fe^{3+} ions into g-C_3N_4 can generate a stable nitrogen-metal hybrid macrocyclic material by means of complexing with the hepta-nitrogen ring, which has six nitrogen lone pair electrons in g-C_3N_4 [26,27]. Besides, Fe^{3+} ions can be included in the "nitrogen tank" structure of g-C_3N_4 through coordination with the amide group. Then, the Fe-N_x bond, a key active site of ferric ion-doped graphite carbon nitride (Fe–CN-3), is formed [28]. In addition to promoting interfacial electron transfer, inducing intrinsic electrons, and energy band modulation, Fe^{3+} coordination doping can passivate the carbon position of the triazine ring and prevent the formation of g-C_3N_4 crystals, which favored the formation of excited electronic transition states of Fe–CN-3 [29,30]. In summary, it can be expected that Fe–CN-3 will exhibit improved ECL performance in comparison with that of g-C_3N_4.

Nanoquencher-based biosensors have better sensitivity and stability in detecting nucleic acids, proteins, metal ions, etc. Therefore, biosensors based on nanoquencher are continuously being developed, such as Au@UiO66-NH_2, Bi_2S_3 nanorods, Si_2O@PDA [31–33]. In this paper, Cu_2O was used as a quenching probe, thus improving the sensor performance. As a p-type semiconductor, cuprous oxide (Cu_2O) has the benefits of easy synthesis, non-toxicity, low cost, and high abundance. Moreover, due to its versatile physicochemical features, it is also one of the transition metal oxide crystals that has been the subject of the most current study [34,35]. In addition, due to its regular cubic morphology, good biocompatibility, and high specific surface area, Cu_2O nanoparticles functionalized through an amination reaction were designed here to combine with the second antibodies of Cyfra21-1. Above all, it was discovered that there was a clear match between the ECL emission spectrum of Fe–CN-3 and the ultraviolet–visible spectrum of absorption of Cu_2O, which allowed the ECL-RET interaction to occur between Cu_2O and Fe–CN-3. Consequently, the ECL signal of Fe–CN-3 can be suppressed by Cu_2O well [36].

In this study, the novel ECL-RET donor-receptor pair with excellent properties were used for immunosensor construction, which enabled the ultrasensitive analysis of Cyfra21-1. The modified carbon nitride Fe–CN-3, which combines the advantages of shape modulation and ion doping, was used as an ECL donor for the first time, which not only incorporates the benefits of carbon nitride materials, but also provides more reactive sites and faster electro-charge migration and separation compared with g-C_3N_4, thus possessing the advantages of better stability and stronger ECL emission. The ECL receptor is an easy-to-synthesise Cu_2O nanocubes, which binds well to the antibody and exhibits efficient and stable quenching effect on Fe–CN-3, improving the sensitivity and selectivity of the sensor. This research may offer a fresh theoretical foundation and methodological guide for the medical investigation of numerous additional biomarkers.

2. Experimental section

2.1. Synthesis of Fe–CN

Fe–CN with different ferric ion doping amounts were synthesized based on the reported method with slight modifications [37]. Specifically, 40 mL of water was boiled to 100 °C. After that, concentrated hydrochloric acid (2 mL), melamine (2000 mg), and $FeCl_3{\cdot}6H_2O$ (61.8 mg) were introduced under vigorous stirring. Next, evaporate the solution to dryness at 100 °C to get rid of water. Finally, the acquired powder was positioned at a porcelain boat wrapped in tin foil and calcined in a nitrogen atmosphere at 550 °C for 6 h to obtain Fe–CN, named Fe–CN-3 (the feeding amount of $FeCl_3{\cdot}6H_2O$ accounted for 3 % of the total solid material). In addition, Fe–CN-1, Fe–CN-5, Fe–CN-6, Fe–CN-7, and Fe–CN-9 were also synthesized according to the same operation except for changing the amount of $FeCl_3{\cdot}6H_2O$.

2.2. Preparation of Fe–CN-3-Ab_1

15 mg of Fe–CN-3 was added into phosphate buffered saline (PBS) solution (5 mL, pH 7.4) containing EDC (191 mg) and NHS (291.7 mg). After ultrasonic mixing, 250 μL of Ab_1 (10 μg/mL) was put to the aforementioned solution and incubated at 4 °C overnight. The solution was then centrifuged and re-dispersed in PBS solution (5 mL, pH 7.4). Finally, the prepared Fe–CN-3-Ab_1 solution was chilled to 4 °C in preparation for usage.

2.3. Synthesis of Cu_2O nanocubes

Cu_2O nanocubes were created with a few modest modifications to the prior instructions [38]. Firstly, solution A was produced by dissolving 0.25 mM (0.05 g) $Cu(CH_3COO)_2{\cdot}H_2O$ and 0.005 mM of PVP (K30) in water (100 mL), and then sodium hydroxide (5 mM) was dispersed to form solution B in water (20 mL), followed by dissolving 0.75 mM of ascorbic acid in water (15 mL) to prepare solution C. Secondly, a blue suspension was created by adding solution B dropwise to solution A and rapidly stirring at ambient temperature. Thirdly, drop by drop, solution C was added to the suspension above while being vigorously stirred. Finally, the obtained orange-yellow suspension was centrifuged, rinsed three times with water, and then vacuum-dried at 60 °C for the entire night.

2.4. Preparation of Cu_2O-Ab_2

In the first place, 10 mL of ethanol was applied to disper 0.1 g of Cu_2O. After addition of 0.1 mL of (3-aminopropyl) triethoxysilane (APTES), the mixture was refluxed for 1.5 h at 70 °C. After centrifugation, washing, and drying, ammonized Cu_2O (Cu_2O–NH_2) was obtained.

In the first place, PBS solution (2 mL, pH 7.4) was used to mix with 100 μL of Ab_2 solution (10 μg/mL) followed by adding EDC (76.4 mg) and NHS (116.68 mg). Stirring for 4 h at 4 °C was followed by the addition of 3 mg of Cu_2O–NH_2, then stirring for another 12 h. Lastly, the nonspecific binding sites were occupied with 100 μL of 0.1 % bovine serum albumin (BSA). After centrifugation and washing, the obtained Cu_2O-Ab_2 precipitate was dispersed in 2 mL of PBS solution (pH 7.4), which was then stored for later use at 4 °C.

2.5. Construction of quenched biosensor

Fig. 1 showed the manufacturing process of the sandwich-quenched electrochemical luminescence biosensor. Firstly, a 0.05 μm alumina slurry was used to polish glassy carbon electrode (GCE, $\Phi = 4$ mm) to get a clean surface. Secondly, 6 μL of Fe–CN-3-Ab_1 (3 mg/mL) solution was attached, allowed by BSA (0.1 %, 3 μL) to occupy the non-specific adsorption sites. Thirdly, the varying concentrations of Cyfra21-1 antigen (6 μL) were applied onto the electrode surface. Finally, after the immune recognized association of a 6 μL Cu_2O-Ab_2 solution (2 mg/mL), the sensor was developed and stored for subsequent use at 4 °C.

2.6. ECL detection

80 mM KCl and 80 mM $K_2S_2O_8$ were dissolved into a pH 7.4 of PBS solution to derive the co-reactant mixture for the ECL measurement. As the electrochemiluminescence sensor, the chemiluminescence detector's chamber was connected to the Ag/AgCl reference electrode, the prepared working electrode, and the platinum wire counter electrode. The electrochemical workstation and the chemiluminescence detector were connected. The photomultiplier tube was configured with a high voltage of 600 V, a scan rate of 0.15 V/s, and a scan voltage of −1.6–0 V.

3. Results and discussion

3.1. Characterization of materials

In this study, Fe^{3+} and nitrogen atoms in the "nitrogen tank" and amide groups of g-C_3N_4 interacted to dope Fe^{3+} into the g-C_3N_4 framework. The partial structure chart of the molecule before and after doping was shown in Scheme 1. SEM, EDS, and XPS methods were used to describe the composition and morphology of Fe–CN. Fig. S1 and Fig. 2showed the SEM photos of g-C_3N_4 and Fe–CN-3 composites. The original g-C_3N_4 showed a dense bulk structure (Fig. S1A), while the morphology of Fe–CN-1 presented a fluffy, lumpy structure (Fig. S1B). At the same time, Fig. 2A showed that Fe–CN-3 was a flower-like structure composed of large and thin lamellae. With increasing Fe^{3+} doping levels, the lamellae structure became thicker until the lamellae became less pronounced (Fig. S1C ~1F). The EDS results of flower-like Fe–CN-3 demonstrated that Fe^{3+} was successfully inserted into the g-C_3N_4 framework (Fig. 2B and C). The morphology and composition of Fe–CN affect its ECL properties. This is because the rigid two-dimensional skeleton of metal-free carbon nitride can effectively reduce the occurrence of non-radiative leaps. With the introduction of

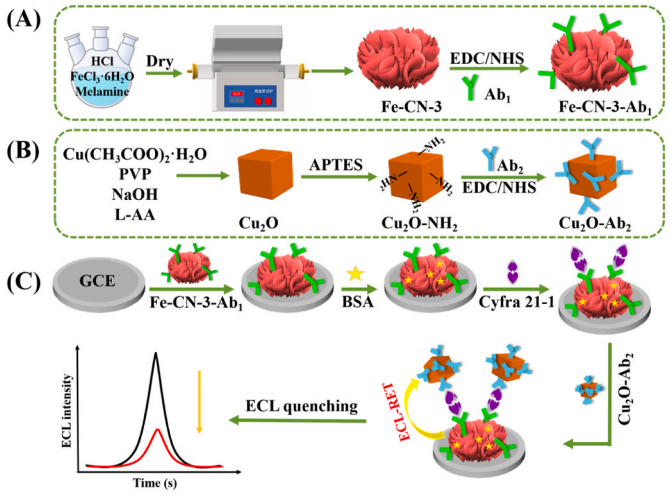

Fig. 1. Synthesis of the materials and construction process of ECL immunosensor.

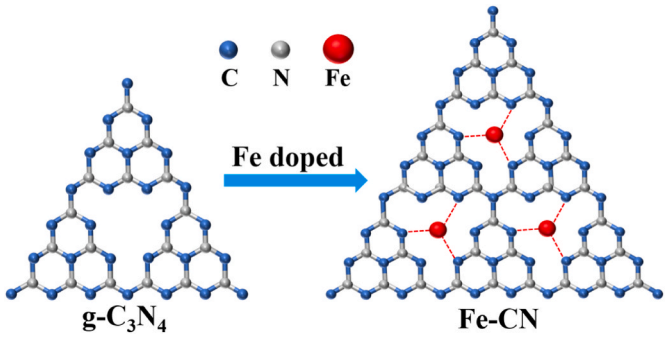

Scheme 1. The schematic diagram of introduction of Fe^{3+} into g-C_3N_4 framework.

Fe^{3+}, the morphology of g-C_3N_4 gradually transitions from a bulk structure to a two-dimensional structure. However, excessive doping will make the structure disappear, and the intensity of the ECL signal will trend upward and then downward. The changes in the morphology and composition enhance the intensity of the ECL signal, thereby improving the sensor's sensitivity and detection range. Thus, the sensitivity and detection range of the sensor are enhanced. Additionally, Fig. 2D displayed the Cu_2O SEM picture, which illustrated that Cu_2O 200–300 nm in dimensions, typical square in shape, with a sleek exterior. Cu_2O nanocubes with regular morphology are easy to combine with secondary antibodies to form secondary antibody markers, which makes the sensors easy to construct, and due to their excellent quenching performance for luminophores, the sensors have lower detection limits and higher sensitivity. Meanwhile, the excellent biocompatibility better maintains the activity of the antigen-antibody.

The corresponding semaphores of elements C, N, and O can be noticed in the XPS spectrum of Fe–CN-3 (Fig. 3A), indicating that the main components of Fe–CN-3 are C and N. The presence of the O 1s signal in the general spectrum may be caused by the outermost layer of the Fe–CN-3 catching molecules of O_2 or H_2O molecules by the Fe–CN-3 surface. The two peaks of the C 1s spectrum in Fig. 3B, which represent the C atom in the C–N bond, N–C═N bond, or C–$(N)_3$ bond, which are 284.8 eV and 288 eV [30]. In Fig. 3C, the peak of N 1s is decomposed into four distinct surges located at 404.53 eV, 400.86 eV, 399.63 eV, and 398.65 eV, which corresponded to amino functional groups (C–NH_2 or C═NH), connecting nitrogen atoms (N–$(C)_3$), Fe–N bonds, and sp^2 hybridized N atoms within the tri-*s*-triazine ring (C–N═C), correspondingly [26]. In Fig. 3D, the peaks centered at 711.2 eV belonged to Fe 2p [29]. The binding energy of 711.2 eV is very close to the previous reports, [39] in

which the Fe species was stabilized in the electron-rich g-C_3N_4 structure through Fe–N bonds. In short, These outcomes indicated that Fe–CN-3 had been successfully synthesized and the Fe^{3+} were connected to the N atom by Fe–N coordinate bonds.

Between 500 and 4000 cm^{-1} in wavelength, the functional groups of the flower-like Fe–CN materials that were produced and bulk g-C_3N_4 were characterized by the Fourier transform infrared (FT-IR) spectroscopy. As seen from Fig. S2, all samples showed several similar peaks as follows. The band at 806 cm^{-1} represented a typical tri-*s*-triazine bending vibration. The peak in the 1200–1700 cm^{-1} region was found to be caused by the aromatic ring's C–N bond stretching vibration. However, it was noteworthy that in the spectra of the flower-liker Fe–CN samples, the intensity of the band 2173 cm^{-1}, which has to do with C≡N's stretching vibration, increased with the quantity of Fe doping and moved towards higher wavelengths, which suggested that during the doping procedure, a chemical link was formed between the atoms of Fe and N. Additionally, N–H bond stretching vibrations were identified as the source of the tiny peak at 887 cm^{-1}. In contrast, large absorption peaks appeared at 3000–3600 cm^{-1} were identified as either hydroxy stretching vibrations of adsorbed water molecules or stretching

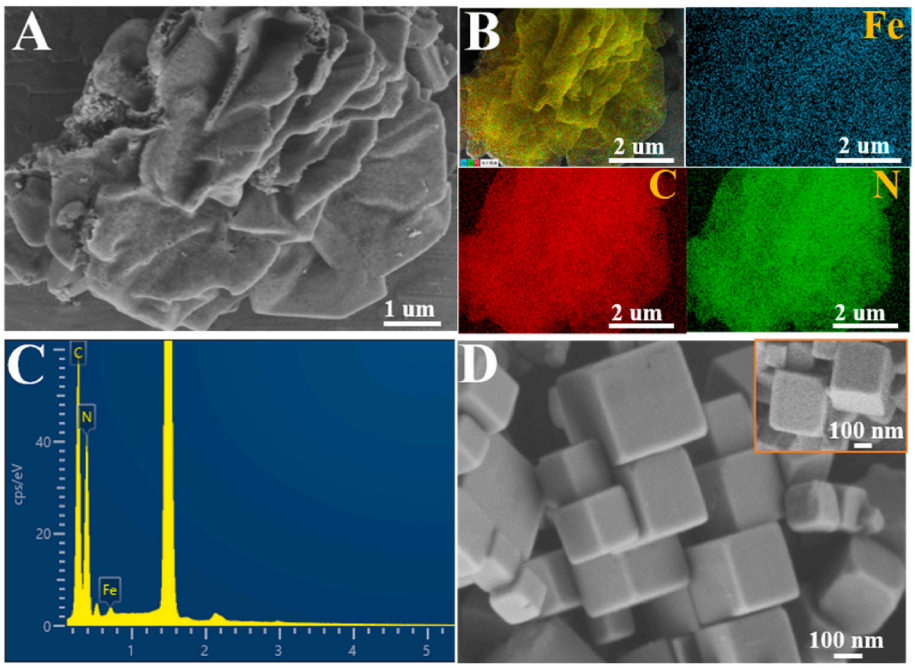

Fig. 2. (A) SEM images of Fe–CN-3, (B) EDS images of Fe–CN-3, (C) Mapping images of Fe–CN-3, (D) SEM images of Cu_2O.

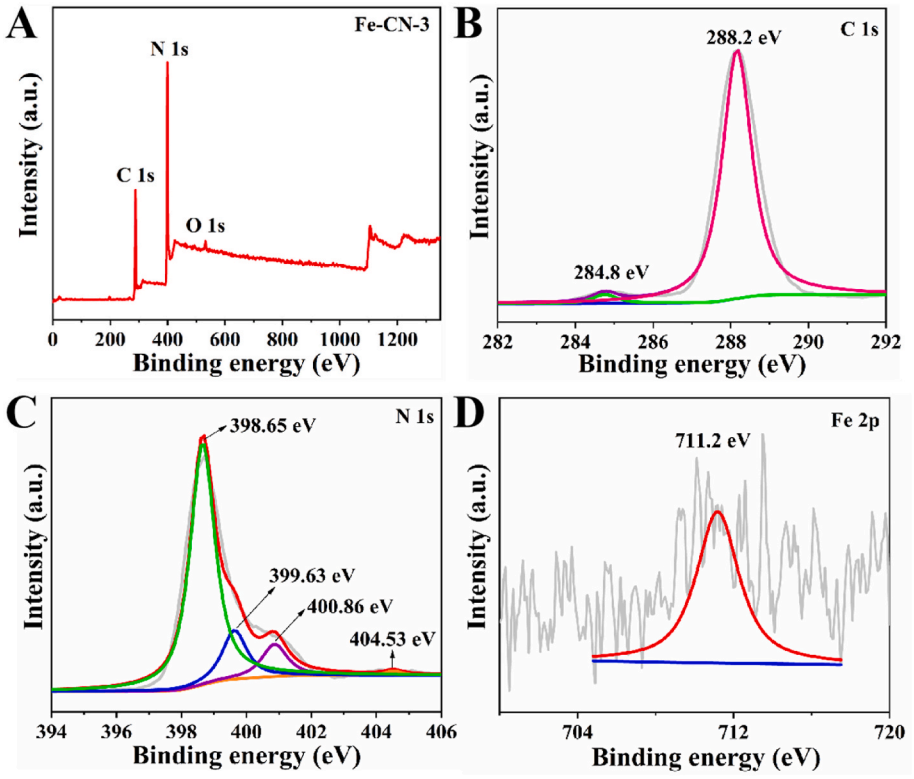

Fig. 3. (A) XPS patterns of Fe–CN-3, (B) C 1s XPS patterns of Fe–CN-3, (C) N 1s XPS of patterns Fe–CN-3 and (D) Fe 2p XPS patterns Fe–CN-3.

vibrations of amino groups. The amino groups were to blame for the decrease of the peaks at these two sites, with the increasing Fe doping coordinating with Fe^{3+} to form complexes, which further confirmed that Fe^{3+} was doped into g-C_3N_4 by coordination interaction. Moreover, Fe–CN with different amounts of Fe doping showed comparable bulk g-C_3N_4 characteristic absorption peaks, suggesting that the chemical structure of g-C_3N_4 remains unchanged upon the addition of the Fe element, which was consistent with the literature [37,40]. Fig. 4A shows the infrared spectra of g-C_3N_4, Fe–CN-3 and Fe–CN-3-Ab_1. The peak pattern of the antibody-modified Fe–CN-3 was changed in the range of 1518–1673 cm^{-1}, the peak intensity was weakened, and there was also the appearance of new peaks, which may be due to the stretching vibration of the C═O bond in the structure of the antibody. At the same time, it is also the characteristic of amide I and amide II bonds in the

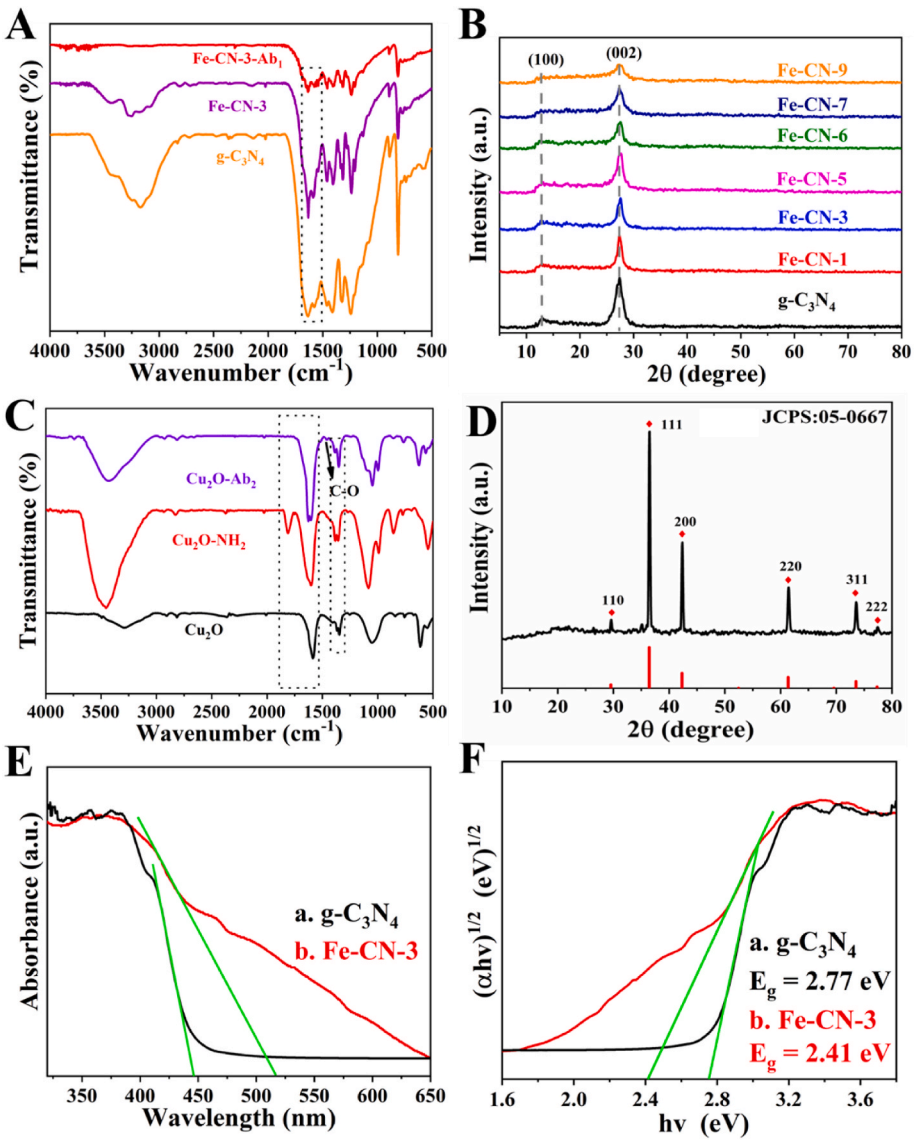

Fig. 4. (A) FT-IR spectra of g-C_3N_4, Fe–CN-3 and Fe–CN-3-Ab_1; (B) XRD patterns of bulk g-C_3N_4 and Fe–CN with different Fe doping amounts; (C) FT-IR spectra of Cu_2O, Cu_2O–NH_2 and Cu_2O-Ab_2; (D) XRD patterns of Cu_2O; (E) UV–vis diffuse reflectance absorption spectra and (F) bandgap spectra of g-C_3N_4 (black) and Fe–CN-3 (red).

structure of proteins. The peaks of –OH and –NH_2 at 3000–3600 cm^{-1} were extremely weak, indicating that –NH_2 in Fe–CN-3 was coupled with the carboxyl group of the antibody. The above structure strongly confirms the successful connection of the luminophore with the material [41,42].

Fig. 4B illustrated that the XRD diffraction peak locations of flower-like Fe–CN and bulk g-C_3N_4 appeared almost identical. To be specific, the in-plane reflection of the tri-*s*-triazine ring, which corresponds to the (100) diffraction plane, was identified as the cause of the weaker diffraction peak at 12.8°. The (002) crystal plane was responsible for the interlayer stacking of conjugated aromatic rings, which was represented by another stronger diffraction peak at 27.0°. When the amount of Fe doping in Fe–CN increases, the peak intensity of the (100) crystal plane gradually drops to almost nonexistent upon comparison with bulk g-C_3N_4. This suggests that Fe was fixed in the g-C_3N_4 frame by the coordination link Fe−N_X. Similarly, as the amount of Fe doping increased, the peak intensity at 27.0° corresponded to the (002) crystal plane, also considerably dropped, indicating that the host-guest interaction and the inhibition of polymer condensation through the introduction of ferric ion species destroyed the fundamental units' periodic arrangement in g-C_3N_4. Moreover, no other iron oxide peaks were found, which was consistent with previous studies [30,37]. This indicated that Fe^{3+} had been successfully incorporated into the g-C_3N_4 structure. Therefore, the XRD data confirmed that the Fe–CN preparation was successful.

The FT-IR spectra of Cu_2O, Cu_2O–NH_2 and Cu_2O-Ab_2 were shown in Fig. 4C. The Cu–O stretching vibration in Cu_2O was indicated by the peak in the Cu_2O spectrum that occurs at 500 to 600 cm^{-1}. Also, the Cu–*O*–H bond's bending vibrational mode was linked to the wide peak at 1000 cm^{-1}. The peaks approximately 1500 cm^{-1} and 3000–3500 were the O–H bond stretching modes in adsorbed H_2O molecules [34]. In addition to the characteristic peaks of Cu_2O, many new peaks have been found in the Cu_2O–NH_2 spectrum. The stretching vibrations of amino groups or hydroxyl groups in the adsorbed water correlate to the peaks at 3000–3700 cm^{-1}. However, the stretching vibrations of Si–*O*–Si and Si–*O*–C are represented by new peaks at 1114, 1806 and 500 cm^{-1}, respectively. These new characteristic mounts indicate the successful amination of Cu_2O [43]. The IR absorption peaks of Cu_2O-Ab_2 at 1540–1890 cm^{-1} are completely different from those of Cu_2O and Cu_2O–NH_2, not only the peaks are shifted, but also new IR absorption peaks appear at 1640 cm^{-1}, which is a result of the influence of the

characteristics of amide I (C═O, C–N stretching and N–H bending). Meanwhile, Cu_2O-Ab_2 had a newly appeared weak characteristic absorption peak at 1245 cm^{-1}, which was caused by the stretching of the C–O bond, and in the range of 1330–1500 cm^{-1}, the peak shape and the peak value changed weakly, which might originate from the changes caused by the amide III bond, and the fingerprint area also showed different absorption peaks, and all the above results strongly confirmed the successful binding of the secondary antibody to Cu_2O [42,44].

Fig. 4D showed the XRD pattern of Cu_2O. The diffraction peaks and diffraction crystal planes of Cu_2O were consistent with the standard card (JCPS: 05–0667), with features at 77.4°, 73.56°, 61.4°, 42.32°, 36.44° and 29.56° correspond to the (222) crystal planes of Cu_2O, (311), (220), (200), (111) and (110), respectively. The above results indicated that the synthesized substance was Cu_2O with a cubic structure centered at the surface.

The DRS measurements of g-C_3N_4 and Fe–CN-3 were carried out. The g-C_3N_4 spectrum (black curve) in Fig. 4E shows that the absorption edge emerged at about 450 nm. On the other hand, Fe–CN-3's UV–visible absorption edge was redshifted when compared to pure g-C_3N_4. These findings suggested that g-C_3N_4's intrinsic electrical and energy band structure might be modulated by Fe^{3+} doping, and the absorption edge's redshift lowered the energy that caused the electron transition of Fe–CN-3. The formula $\alpha h\nu = A\ (h\nu - E_g)^{n/2}$ can be applied to compute the band gap energy. In this formula, α stands for absorption coefficient, h for Planck's constant, E_g for energy band gap, ν for optical frequency, A for continuous, and $n/2$ for semiconductor photo transition type [45]. g-C_3N_4 and Fe–CN-3 were found to have band gaps of 2.77 eV and 2.40 eV, separately, based on the comparison between $(\alpha h\nu)^{1/2}$ and $h\nu$ in Fig. 4F. It was obvious that the band gap width of Fe–CN-3 was reduced by 0.35 eV in contrast to g-C_3N_4. This could enhance the electron transfer capability and make it easier to create excited states.

The BET specific surface area and pore information of pristine g-C_3N_4 and Fe–CN-3 were analysed by N_2 absorption/desorption method. Figs. S3A and B show the type IV isotherms and H4 hysteresis loops of the respective two, indicating the presence of a pore structure in the samples, with surface areas of 33.86 m^2/g (g-C_3N_4) and 68.85 m^2/g (Fe–CN-3), respectively. The results demonstrated that Fe doping can enhance the specific surface area and 3–13 nm pore distribution of g-C_3N_4, the large specific surface area makes the luminophore contact with more co-reactants, and the higher porosity can promote the diffusion of co-reactants into the layers of luminescent materials on the surface of the electrodes, thus generating more Fe–CN-3* in the excited state, and improving the luminescence performance of Fe–CN-3.

3.2. ECL emission behavior and Cu_2O quenching mechanism of Fe–CN/$K_2S_2O_8$ system

The ECL performance of six Fe–CN nanocomposites with varying levels of Fe doping were investigated and the results were displayed in Fig. S4. Fe–CN-3 exhibited a more robust and consistent ECL signal in comparison to the other Fe–CN nanocomposites. This might be due to the fact that the flower-liked structure of Fe–CN-3 with large and thin lamellae made more ECL emitting groups inside the structure to be exposed and activated than that of other Fe–CN. In addition, the quenching performance of Cu_2O was examined, and Fig. 5A displays the findings. The g–C_3N_4–modified electrode's ECL signal was extremely weak (curve b), while the un-modified bare electrode (curve a) exhibited nearly no ECL emission under the same test circumstances. However, the Fe–CN-3-modified electrode (curve c) exhibited a remarkable ECL signal. This result further demonstrated that Fe doping can meaningfully enhance the g-C_3N_4' ECL performance. After further modification of Cu_2O onto the working electrode (curve d), the ECL intensity sharply dropped, suggesting that Cu_2O had an obvious quenching effect on the Fe–CN-3 ECL signal.

Functionalization or control of the carbon nitride synthesis process can only modulate its ECL properties but not change its ECL mechanism [46]. So far, the ECL phenomenon in g-C_3N_4 has been based on the co-reactant pathway, where at the cathodic potential, the co-reactants produce intermediates that react with the free radicals of g-C_3N_4 to produce excited states [16,47]. Relies on the luminescence behavior of Fe–CN-3 and g-C_3N_4, the possible ECL mechanism for Fe–CN-3 were discussed. Concrete term, when the electrode voltage was swept from

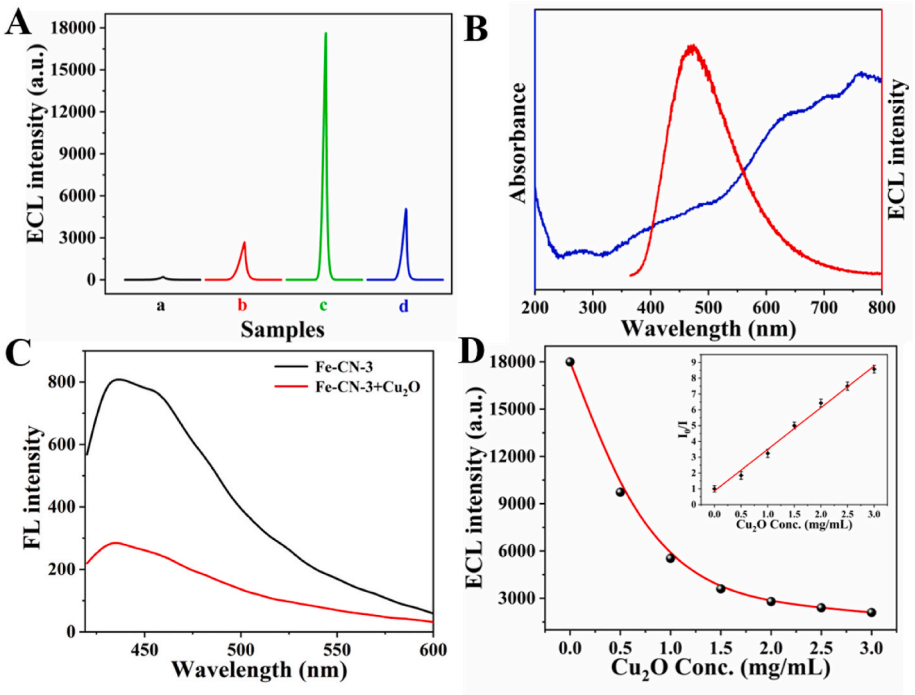

Fig. 5. (A) ECL behaviors of bare GCE (a), GCE/g-C_3N_4 (b), GCE/Fe–CN-3 (c) and GCE/Fe–CN-3/Cu_2O (d) in PBS (pH 7.4, 80 mM $K_2S_2O_8$); (B) ECL emission spectra of Fe–CN-3 (red) and UV–Visible light absorption spectrum of Cu_2O (blue); (C) The fluorescence spectra of Fe–CN-3 (black) and a mixture of Fe–CN-3 and Cu_2O (red); (D) quenching effect of Cu_2O and calibration curve of Cu_2O detection (cut line). Error bars = RSD (n = 5).

−1.6 to 0 V, Fe–CN-3 was first oxidized to Fe–CN-3$^{\bullet-}$ after gaining electrons (Equation (1)). Meanwhile, $S_2O_8^{2-}$ was oxidized to $SO_4^{\bullet-}$ after gaining electrons (Equation (2)). Next, the strong oxidant $SO_4^{\bullet-}$ reacted with Fe–CN-3$^{\bullet-}$ to form Fe–CN-3* (Equation (3)). Finally, when Fe–CN-3* transformed back into photons and went from the excited state to the ground state, a powerful emission light quench forth (Equation (4)). [48].

$$\text{Fe–CN-3} + e^- \rightarrow \text{Fe–CN-3}^{\bullet-} \quad (1)$$

$$S_2O_8^{2-} + e^- \rightarrow SO_4^{2-} + SO_4^{\bullet-} \quad (2)$$

$$\text{Fe–CN-3} + SO_4^{\bullet-} \rightarrow \text{Fe–CN-3*} + SO_4{}^{2-} \quad (3)$$

$$\text{Fe–CN-3*} \rightarrow \text{Fe–CN-3} + h\nu \quad (4)$$

The ECL quenching mechanism was further studied and the findings are displayed in Fig. 5B. The ECL emission spectrum of Fe–CN-3 (red curve) illustrated that the luminescence range was at 400–600 nm, 440 nm from the highest peak. Moreover, a broad absorption in the 350–800 nm wavelength range was seen in the UV–vis absorption spectrum of Cu_2O (blue curve). It was noteworthy that the ECL emission spectrum of Fe–CN-3 and the UV–vis spectrum of Cu_2O showed a discernible overlap. It manifested that an ECL-RET interaction from Fe–CN-3 (energy donor) to Cu_2O (energy acceptor) occurred. In addition, to learn more about Cu_2O's quenching capacity, the fluorescence spectra of Fe–CN-3 and its mixes with Cu_2O were recorded. Fe–CN-3's greatest emission peak was at 430 nm, with an 800 a.u. fluorescence intensity (black curve), as seen in Fig. 5C. However, when mixing with Cu_2O, the fluorescence emission intensity at 430 nm decreased significantly (red curve), indicating that Cu_2O can inhibit the fluorescence emission of Fe–CN-3.

For the purpose of further investigating the quenching performance of the Cu_2O quencher, a series of concentrations of Cu_2O were used to explore the ECL quenching experiment towards Fe–CN-3 in 10 mL PBS dissolved with 80 mM $K_2S_2O_8$ and KCl. And the obtained results were shown in Fig. 5D. The linear relationship between I_0/I and Cu_2O concentrations is depicted inside Fig. 5D. The ECL intensity constantly lowers as Cu_2O concentration rises. I and I_0 represented the ECL intensity in this stage with and without Cu_2O, respectively. The quenching constant (K_{sv}) based on the fitted curve, as determined by the Stern-Volmer equation: $I_0/I = 1 + k_q\tau_0[Q] = 1 + K_{sv}[Q]$, was 0.865×10^5 g^{-1} in the 0–3.0 g/L range ($R^2 = 0.993$). All the above results confirmed that Cu_2O has excellent quenching properties.

3.3. Improvement of the test condition

Based on the ECL strength and stability, the co-reactive reagent concentration, quenched material concentration, substrate concentration, and pH were adjusted to obtain the maximum detection efficiency. As seen in Fig. 6A, the concentration of Fe–CN-3 and the ECL intensity had a positive correlation when Fe–CN-3 concentration was below 3 mg/mL, but was negatively correlated when Fe–CN-3 concentration was above 3 mg/mL. So, Fe–CN-3 at a 3 mg/mL concentration was the ideal level. Furthermore, $K_2S_2O_8$ concentration was also improved. As Fig. 6B illustrates, as the concentration of $K_2S_2O_8$ increased, so did the ECL intensity in cases where the $K_2S_2O_8$ concentration was below 80 mM. In cases where the $K_2S_2O_8$ concentration exceeded 80 mM, as the concentration of $K_2S_2O_8$ increased, the ECL intensity dropped. As a result, the optimal concentration of the co-reactant $K_2S_2O_8$ was chosen to be 80 mM. Since the reaction between antigen and antibody only occurs in a suitable pH environment, the pH value of the test solution was subsequently explored. The ECL emission intensity peaked at pH 7.4 when screening was performed from pH 6.0 to 8.5, as Fig. 6C illustrates. Hence, 7.4 was determined to be the ideal pH level. Finally, the ideal quenching effect was obtained by optimizing the quantity of Cu_2O. It can be seen from Fig. 6D, the quenching effect showed an upward trend when Cu_2O concentrations was below 1.5 mg/mL. Upon exceeding 1.5 mg/mL of Cu_2O, the quenching effect remained almost unaltered. Therefore, 1.5 mg/mL was the ideal quenching agent concentration.

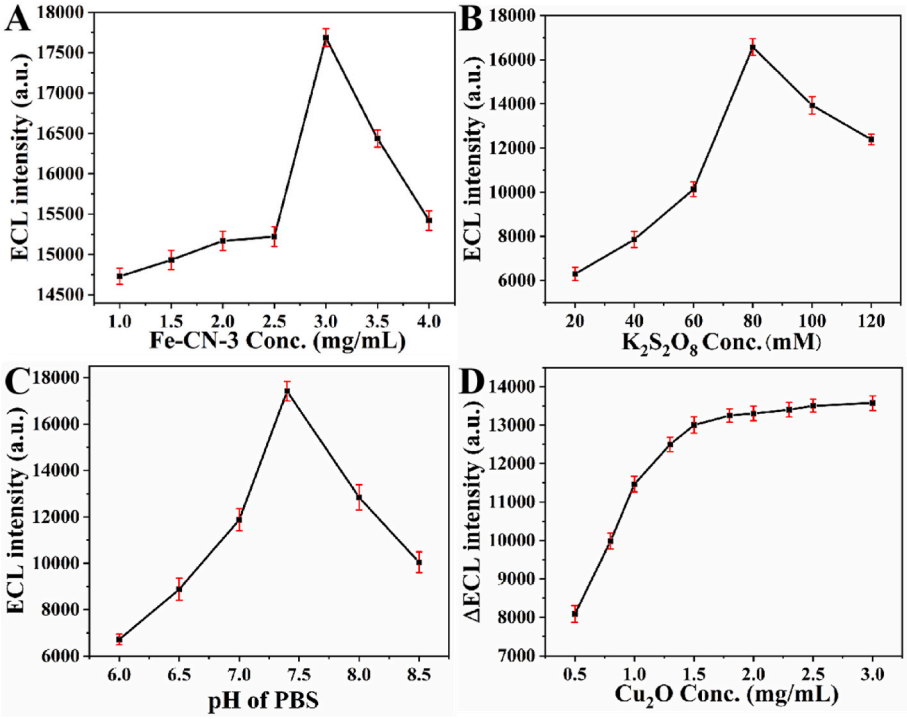

Fig. 6. The effects of (A) Fe–CN-3 concentration, (B) $K_2S_2O_8$ concentration and (C) pH of PBS on ECL intensity; (D) The quenching impact of various Cu_2O concentrations on the ECL signal corresponding to 1 ng/mL Cyfra21-1 detected by the immunosensor (ΔECL was the difference between GCE/Fe–CN-3-Ab_1/BSA/Cyfra21-1 and GCE/Fe–CN-3-Ab_1/BSA/Cyfra21-1/Cu_2O-Ab_2). Error bars = RSD ($n = 5$).

3.4. Characterization of the constructed ECL sensor

The relationship between the voltage of the electrodes and the ECL intensity was investigated to show how the immunosensor is constructed. The findings are displayed in Fig. 7A. The ECL signal of the bare electrode was weak (curve a). When the Fe–CN-3-Ab_1 compound was altered on GCE (curve b), the ECL intensity reached the maximum. After BSA (curve c) and Cyfra21-1 (curve d) were gradually added to the working electrode, the ECL intensity steadily dropped, possibly as a result of protein molecules impeding electron transit. Finally, after modification of Cu_2O-Ab_2 (curve e), the ECL signal reached the minimum, demonstrating the Cu_2O-Ab_2 quenching probe's remarkable quenching efficiency. The immunosensor was successfully constructed, as evidenced by the above results.

Moreover, the immunosensor's building process was further demonstrated by electrochemical impedance spectroscopy (EIS) tests conducted on several modified electrodes in solutions containing 2.5 mM $[Fe(CN)_6]^{3-/4-}$ and 0.1 M KNO_3 (Fig. 7B). The inset equivalent circuit can be used to simulate Nyquist plots. Table S1 displayed the relevant values that the ZSimpWin software simulated. Of these parameters, the most notable is the change in the charge transfer and redox reaction resistance (R_{et}), which demonstrated the electroactive marker's diffusion retardation at the electrode interface. The bare electrode displayed a little semicircle (curve a), as seen in Fig. 7B, indicating that electrons can be transferred almost freely. Since Ab_1's non-conductive nature as a biomaterial, the semicircle diameter increased when Fe–CN-3-Ab_1 was applied to the surface of the electrode (curve b). The diameter of the semicircle kept growing with stepwise modification of non-conductive BSA (curve c) and Cyfra21-1 antigen (curve d). In the end, the R_{et} value reached the maximum when Cu_2O-Ab_2 was further modified onto the working electrode, which verified the immunobinding between the antigen and the Ab_2 biomarker. The quenching ECL immunosensor was successfully constructed, as seen by the cyclic voltammetry (CV) curves in Fig. S5, which matched all of the previously reported results.

3.5. Analytical ability of the constructed sensor

For evaluating the sensing property of the constructed immunosensors, the ECL strengths of Cyfra21-1 at different concentrations were determined under optimal experimental conditions. Fig. 7C demonstrated that the ECL intensity steadily decreased as the concentration of Cyfra21-1 rose from 0.00005 ng/mL to 100 ng/mL. The corresponding calibration curve was depicted in Fig. 7D, and the equation for linear regression $I_{ECL} = 3719.7–901.5 \times \lg c$ ($R^2 = 0.995$) was credible. Here, it was determined that the limit of detection (LOD) was 17.4 fg/mL (S/N = 3). The reduced LOD and larger detection range may be the result of the remarkable ECL emission properties of the flower-like Fe–CN-3 and the prominent quenching effect of Cu_2O, in contrast to other detection strategies (Table S2).

3.6. Immunosensor performance in application

In order to assess the manufactured immunosensors' selectivity, protein indicators that resemble the target antigen, such as alpha-fetoprotein (AFP), human Serum albumin (HSA), prostate specific antigen (PSA), carcinoembryonic antigen (CEA) and B-type natriuretic peptide (BNP), were chosen as potential interfering substances. Based on the results presented in Fig. 8A, there was no discernible effect on the ECL signal when the immunosensors were tested with either blank samples or 1 ng/mL of interfering substance. Also, the ECL strength of the immunosensor was nearly the same whether it was tested with 1 ng/mL Cyfra21-1 alone or in combination with 100 ng/mL of the aforementioned interferents. Based on the results, it was demonstrated that the proposed ECL immunosensor exhibited exceptional selectivity.

Repeatability is an essential factor in the application of immunosensors. Assays intra and inter were carried out to evaluate the sensor's

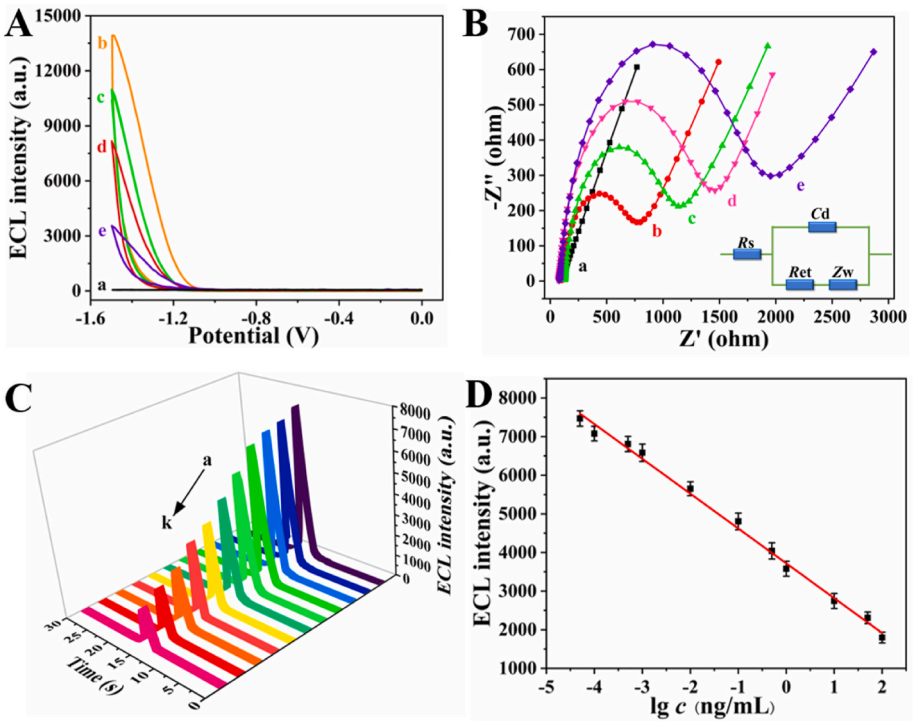

Fig. 7. (A) The ECL intensity-potential curves in PBS (pH 7.4) containing 80 mM $K_2S_2O_8$ and 0.1 M KCl and (B) The corresponding EIS curves in 2.5 mM $Fe(CN)_6^{3-/4-}$ and 0.1 M KNO_3: (a) GCE, (b) GCE/Fe–CN-3-Ab_1, (c) GCE/Fe–CN-3-Ab_1/BSA, (d) GCE/Fe–CN-3-Ab_1/BSA/Cyfra21-1, (e) GCE/Fe–CN-3-Ab_1/BSA/Cyfra21-1/Cu_2O-Ab_2 (the inset in Fig. 7B is the equivalent analog circuit); (C) ECL responses of immunosensors to different concentrations of Cyfra21-1, from a to k: 0.00005, 0.0001, 0.0005, 0.001, 0.01, 0.1, 0.5, 1, 10, 50 and 100 ng/mL; (D) Standard curve of the immunosensor against different concentrations of Cyfra21-1. Error bars = RSD (n = 5).

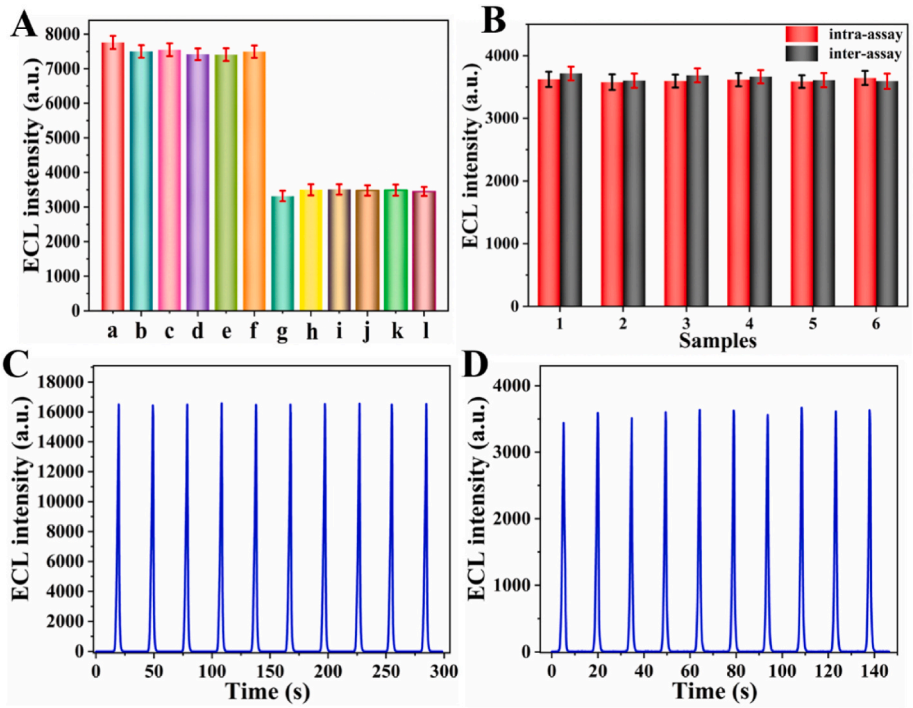

Fig. 8. (A) The selectivity of the constructed ECL immunosensors from a to l: blank, CEA (1 ng/mL), PSA (1 ng/mL), BNP (1 ng/mL), HSA (1 ng/mL), AFP (1 ng/mL), Cyfra21-1 (1 ng/mL), Cyfra21-1 (1 ng/mL), mixture of Cyfra21-1 (1 ng/mL) and PSA (100 ng/mL), mixture of Cyfra21-1 (1 ng/mL) and BNP (100 ng/mL), mixture of Cyfra21-1 (1 ng/mL) and HSA (100 ng/mL), mixture of Cyfra21-1 (1 ng/mL) and AFP (100 ng/mL); (B) Reproducibility of the immunosensor for 1 ng/mL Cyfra21-1 by intra- and inter-assay, error bars = RSD ($n = 5$); Stability tests performed in PBS (pH 7.4) containing 80 mM $K_2S_2O_8$ of (C) Fe–CN-3 and (D) ECL immunosensor for detection of 1 ng/mL Cyfra21-1.

reproducibility. (Fig. 8B). In the same experimental conditions, six electrodes from the same batch (red bars) and six batches of the same electrodes (black bars) had their ECL reactions and responses tested separately. As can be seen from Fig. 8B, the intra- and inter-assay experiment's RSD values were 2.52 % and 1.97 %, respectively. The findings that were mentioned earlier have confirmed that the sensor that was designed has a high level of repeatability.

Good functioning stability is crucial for sensors to be used in real-world applications. First, the stability of flower-like Fe–CN-3 nanomaterial poured onto the surface of the electrode, was detected throughout the course of 10 consecutive scans. The ECL intensity was very stable with an RSD of 0.754 % (Fig. 8C). Similarly, the designed immunosensor applied to detect 1 ng/mL of Cyfra21-1 was constantly scanned for 10 cycles, which displayed good stability with a 1.18 % RSD (Fig. 8D). The aforementioned findings showed that the constructed immunosensor had adequate stability.

3.7. Detection of human serum samples

To investigate this ECL immunosensor's viability for clinical Cyfra21-1 detection in more detail, the recovery rate of serum Cyfra21-1 at various concentrations was determined through the standard addition method. Human serum samples were diluted into three concentrations (1.86, 2.52, and 3.19 ng/mL), and then a series of Cyfra21-1 standard solutions were added to obtain samples to be tested. After testing and calculating, the recoveries had a relative standard deviation of 1.2 %–2.9 % and ranged from 98.3 % to 101.5 % (Table S3). This implied that the constructed immunosensor had a satisfactory recovery rate and potential practical application value.

4. Conclusion

The evolving development of luminescents and quenchers with more superior performance is the key to promote the transition from theory to practice in the field of ECL. Therefore, we have explored the novel luminophore Fe–CN-3, whose satisfactory morphology, specific surface area, and band gap energy promote the electron leaps and the formation of excited states, and improve its ECL performance. It has energised the continued development of carbon nitride in the ECL field. A suitable quenching probe can improve the sensitivity of the sensor, and based on the ECL-RET mechanism, Cu_2O nanocubes were synthesized for quenching the ECL emission of Fe–CN-3. The sensor constructed in this study can be used for the ultrasensitive detection of Cyfra21-1 in the range of 0.00005–100 ng/mL, with a detection limit as low as 17.4 fg/mL. Therefore, the proposed new sensing strategy is of great significance in the diagnosis and detection of lung cancer. However, the constructed sensor still has some deficiencies. For example, the stability of long-time storage needs to be improved, and it is limited to the detection of one disease marker and cannot detect multiple targets at the same time.

CRediT authorship contribution statement

Hao Yu: Writing – original draft, Validation, Software, Methodology, Investigation. **Qianqian Cui:** Writing – original draft, Validation. **Fengdi Li:** Validation. **Yun Wang:** Validation. **Xianpeng Liao:** Validation. **Lihua Hu:** Writing – review & editing, Supervision, Resources, Methodology, Investigation, Funding acquisition, Formal analysis, Conceptualization. **Hongmin Ma:** Methodology. **Dan Wu:** Methodology. **Qin Wei:** Methodology, Formal analysis, Conceptualization. **Huangxian Ju:** Methodology.

Declaration of competing interest

The authors declare that they have no known competing financial interests or personal relationships that could have appeared to influence the work reported in this paper.

Data availability

No data was used for the research described in the article.

Acknowledgements

This study was supported by the National Natural Science Foundation of China (Nos. 21607055, 22274062), National Key Scientific Instrument and Equipment Development Project of China (No.21627809).

Appendix A. Supplementary data

Supplementary data to this article can be found online at https://doi.org/10.1016/j.talanta.2024.126321.

References

[1] X. Yuan, J. Yang, X. Wang, Y. Zhang, H. Yang, X. Wang, Electrochemical impedance analysis of the CYFRA 21-1 antigen based on doxorubicin-initiated ROP signal amplification, New J. Chem. 46 (30) (2022) 14458–14465.
[2] J. Liu, M. Wang, C. Zhang, G. Li, Q. Shen, L. Zou, An ingenious electrochemical aptasensor for detection of CYFRA 21-1 based on dual-output toehold mediated strand displacement reaction, Bioelectrochemistry 147 (2022) 108203.
[3] B. Nakata, T. Takashima, Y. Ogawa, T. Ishikawa, K. Hirakawa, Serum CYFRA 21-1 (cytokeratin-19 fragments) is a useful tumour marker for detecting disease relapse and assessing treatment efficacy in breast cancer, Br. J. Cancer 91 (5) (2004) 873–878.
[4] N.A. Alarfaj, M.F. El-Tohamy, H.F. Oraby, New immunosensing-fluorescence detection of tumor marker cytokeratin-19 fragment (CYFRA 21-1) via carbon quantum dots/zinc oxide nanocomposite, Nanoscale Res. Lett. 15 (1) (2020) 12.
[5] S. Zhang, C. Wang, H. Chi, L. Hu, H. Wang, Q. Wei, D. Wu, A photoelectrochemical biosensor for detecting Cytokeratin-19 fragments based on CdS/Ni$(OH)_2$ core-shell nanosphere composites amplified by CdSe@$MoSe_2$, Sensors and Actuators B-Chemical 360 (2022) 131643.
[6] Y. Cao, J. Feng, L. Tang, G. Mo, W. Mo, B. Deng, Detection of three tumor biomarkers in human lung cancer serum using single particle inductively coupled plasma mass spectrometry combined with magnetic immunoassay, Spectrochimica Acta Part B-Atomic Spectroscopy 166 (2020) 105797.
[7] M.Q. He, K. Wang, W.J. Wang, Y.L. Yu, J.H. Wang, Smart DNA machine for carcinoembryonic antigen detection by exonuclease iii-assisted target recycling and DNA walker cascade amplification, Anal. Chem. 89 (17) (2017) 9292–9298.
[8] M. Kvas, A.G. Teixeira, B. Chiang, J.P. Frampton, Aqueous two-phase system antibody confinement enables cost-effective analysis of protein analytes by sandwich enzyme-linked immunosorbent assay with minimal optical crosstalk, Analyst 145 (16) (2020) 5458–5465.
[9] L. Qu, L. Yang, Y. Li, X. Ren, H. Wang, D. Fan, X. Wang, Q. Wei, H. Ju, Dual-signaling electrochemical ratiometric method for competitive immunoassay of CYFRA21-1 based on urchin-like Fe_3O_4@PDA-Ag and $Ni_3Si_2O_5(OH)_4$-Au absorbed methylene blue nanotubes, ACS Appl. Mater. Interfaces 13 (4) (2021) 5795–5802.
[10] J. Miao, K. Du, X. Li, X. Xu, X. Dong, J. Fang, W. Cao, Q. Wei, Ratiometric electrochemical immunosensor for the detection of procalcitonin based on the ratios of SiO_2-Fc-COOH-Au and UiO-66-TB complexes, Biosens. Bioelectron. 171 (2021) 112713.
[11] Z.H. Yang, S. Ren, Y. Zhuo, R. Yuan, Y.Q. Chai, Cu/Mn double-doped CeO_2 nanocomposites as signal tags and signal amplifiers for sensitive electrochemical detection of procalcitonin, Anal. Chem. 89 (24) (2017) 13349–13356.
[12] J. Wang, X. Jiang, H. Han, Turn-on near-infrared electrochemiluminescence sensing of thrombin based on resonance energy transfer between CdTe/CdS coresmall/shellthick quantum dots and gold nanorods, Biosens. Bioelectron. 82 (2016) 26–31.
[13] S. Xiao, X. Wang, C. Yang, Y. Jiang, S. Zhen, C. Huang, Y. Li, Electrochemiluminescence resonance energy transfer system based on silver metal-organic frameworks as a double-amplified emitter for sensitive detection of miRNA-107, Anal. Chem. 94 (2) (2022) 1178–1186.
[14] X.L. Fu, F. Hou, F.R. Liu, S.W. Ren, J.T. Cao, Y.M. Liu, Electrochemiluminescence energy resonance transfer in 2D/2D heterostructured g-C_3N_4/MnO_2 for glutathione detection, Biosens. Bioelectron. 129 (2019) 72–78.
[15] X.L. Huo, N. Zhang, H. Yang, J.J. Xu, H.Y. Chen, Electrochemiluminescence resonance energy transfer system for dual-wavelength ratiometric miRNA detection, Anal. Chem. 90 (22) (2018) 13723–13728.
[16] R. Malik, N. Joshi, V.K. Tomer, Functional graphitic carbon (IV) nitride: a versatile sensing material, Coord. Chem. Rev. 466 (2022) 214611.
[17] J.Y. Kang, W. Ha, H.X. Zhang, Y.P. Shi, Sandwich-like, potassium(I) doped g-C_3N_4 with tunable interlayer distance as a high selective extractant for the determination of Ba(II), Talanta 215 (2020) 120916.
[18] M. Pourmadadi, E. Rahmani, M.M. Eshaghi, A. Shamsabadipour, S. Ghotekar, A. Rahdar, L.F.R. Ferreira, Graphitic carbon nitride (g-C_3N_4) synthesis methods, surface functionalization, and drug delivery applications: a review, J. Drug Deliv. Sci. Technol. 79 (2023) 104001.
[19] Y.S. Wudil, U.F. Ahmad, M.A. Gondal, M.A. Al-Osta, A. Almohammedi, R.S. Sa'id, F. Hrahsheh, K. Haruna, M.J.S. Mohamed, Tuning of graphitic carbon nitride (g-C_3N_4) for photocatalysis: a critical review, Arab. J. Chem. 16 (3) (2023) 104542.
[20] S. Hu, L. Ma, J. You, F. Li, Z. Fan, G. Lu, D. Liu, J. Gui, Enhanced visible light photocatalytic performance of g-C_3N_4 photocatalysts co-doped with iron and phosphorus, Appl. Surf. Sci. 311 (2014) 164–171.
[21] M. Majdoub, Z. Anfar, A. Amedlous, Emerging chemical functionalization of g-C_3N_4: covalent/noncovalent modifications and applications, ACS Nano 14 (10) (2020) 12390–12469.
[22] D. Long, W. Diao, X. Rao, Y. Zhang, Boosting the photocatalytic hydrogen evolution performance of Mg- and Cl-doped graphitic carbon nitride microtubes, ACS Appl. Energy Mater. 3 (9) (2020) 9278–9284.
[23] S. Zhu, X. Cao, X. Cao, Y. Feng, X. Lin, K. Han, X. Li, P. Deng, Metal-doped (Fe, Nd, Ce, Zr, U) graphitic carbon nitride catalysts enhance thermal decomposition of ammonium perchlorate-based molecular perovskite, Mater. Des. 199 (2021) 109426.
[24] L. Jiang, X. Yuan, Y. Pan, J. Liang, G. Zeng, Z. Wu, H. Wang, Doping of graphitic carbon nitride for photocatalysis: a reveiw, Applied Catalysis B-Environmental 217 (2017) 388–406.
[25] Z. Zhu, X. Tang, W. Fan, Z. Liu, P. Huo, T. Wang, Y. Yan, C. Li, Studying of Co-doped g-C_3N_4 and modified with Fe_3O_4 quantum dots on removing tetracycline, J. Alloys Compd. 775 (2019) 248–258.
[26] Y. Huang, X. Luo, Y. Du, Y. Fu, X. Guo, C. Zou, Y. Wu, The role of iron-doped g-C_3N_4 heterogeneous catalysts in Fenton-like process investigated by experiment and theoretical simulation, Chem. Eng. J. 446 (2022) 137252.
[27] W. Miao, Y. Liu, X. Chen, Y. Zhao, S. Mao, Tuning layered Fe-doped g-C_3N_4 structure through pyrolysis for enhanced Fenton and photo-Fenton activities, Carbon 159 (2020) 461–470.
[28] X. Wang, M. He, Z. Nan, Effects of adsorption capacity and activity site on Fenton-like catalytic performance for Na and Fe co-doped g-C_3N_4, Separation and Purification Technology 256 (2021) 117765.
[29] G. Liu, G. Dong, Y. Zeng, C. Wang, The photocatalytic performance and active sites of g-C_3N_4 effected by the coordination doping of Fe(III), Chin. J. Catal. 41 (10) (2020) 1564–1572.
[30] Y. Yu, S. Cheng, L. Wang, W. Zhu, L. Luo, X. Xu, F. Song, X. Li, J. Wang, Self-assembly of yolk-shell porous Fe-doped g-C_3N_4 microarchitectures with excellent photocatalytic performance under visible light, Sustainable Materials and Technologies 17 (2018) e00072.
[31] J. Yang, D. Qin, N. Wang, Y. Wu, K. Fang, B. Deng, Aggregation-induced electrochemiluminescence based on a Zinc-based metal–organic framework and a double quencher Au@UiO-66-NH_2 for the sensitive detection of Amyloid β 42 via resonance energy transfer, Anal. Chem. 95 (17) (2023) 7045–7052.
[32] M. Xia, J. Wang, S. Li, A. Lin, Q. Yao, Z. Guo, X. Chen, Q. Chen, X. Chen, A sensitive electrochemiluminescence resonance energy transfer system between Ru-MOFs and Bi_2S_3 for deoxynivalenol detection, Sensor. Actuator. B Chem. 393 (2023) 134192.
[33] B. Xing, W. Zhu, X. Zheng, Y. Zhu, Q. Wei, D. Wu, Electrochemiluminescence immunosensor based on quenching effect of SiO_2@PDA on SnO_2/rGO/Au NPs-luminol for insulin detection, Sensor. Actuator. B Chem. 265 (2018) 403–411.
[34] O.L. Evdokimova, M.E. Belousova, A.V. Evdokimova, T.V. Kusova, A. E. Baranchikov, K.S. Antonets, A.A. Nizhnikov, A.V. Agafonov, Fast and simple approach for production of antibacterial nanocellulose/cuprous oxide hybrid films, Cellulose 28 (5) (2021) 2931–2945.
[35] S. Sun, X. Zhang, Q. Yang, S. Liang, X. Zhang, Z. Yang, Cuprous oxide (Cu_2O) crystals with tailored architectures: a comprehensive review on synthesis, fundamental properties, functional modifications and applications, Prog. Mater. Sci. 96 (2018) 111–173.
[36] L. Hu, T. Shi, J. Chen, Q. Cui, H. Yu, D. Wu, H. Ma, Q. Wei, H. Ju, Dual-quenching electrochemiluminescence resonance energy transfer system from CoPd nanoparticles enhanced porous g-C_3N_4 to FeMOFs-sCuO for neuron-specific enolase immunosensing, Biosens. Bioelectron. 226 (2023) 115132.
[37] J. Shi, X. Bai, L. Xu, X. Jin, X. Shi, P. Jin, Facile preparation of Fe-C_3N_4 heterojunction for enhanced pollutant degradation in Fenton-like process, Journal of Water Process Engineering 46 (2022) 102628.
[38] Y. Bai, T. Yang, Q. Cu, G. Cheng, R. Zheng, Shape control mechanism of cuprous oxide nanoparticles in aqueous colloidal solutions, Powder Technol. 227 (2012) 35–42.
[39] X.C. Wang, X.F. Chen, A. Thomas, X.Z. Fu, M. Antonietti, Metal-containing carbon nitride compounds: a new functional organic-metal hybrid material, Adv. Mater. 21 (2009) 1609–1612.
[40] R. Li, J. Huang, M. Cai, J. Huang, Z. Xie, Q. Zhang, Y. Liu, H. Liu, W. Lv, G. Liu, Activation of peroxymonosulfate by Fe doped g-C_3N_4/graphene under visible light irradiation for Trimethoprim degradation, J. Hazard Mater. 384 (2020) 121435.
[41] E.B. Aydın, M. Aydın, M.K. Sezgintürk, A highly sensitive immunosensor based on ITO thin films covered by a new semi-conductive conjugated polymer for the determination of TNFα in human saliva and serum samples, Biosens. Bioelectron. 97 (2017) 169–176.
[42] A. Roberts, S. Mahari, D. Shahdeo, S. Gandhi, Label-free detection of SARS-CoV-2 Spike S1 antigen triggered by electroactive gold nanoparticles on antibody coated fluorine-doped tin oxide (FTO) electrode, Anal. Chim. Acta 1188 (2021) 339207.
[43] X. Yu, Y. Li, Y. Li, S. Liu, Z. Wu, H. Dong, Z. Xu, X. Li, Q. Liu, An electrochemical amplification strategy based on the ferrocene functionalized cuprous oxide superparticles for the detection of NSE, Talanta 236 (2022) 122865.
[44] J. Waeytens, J. De Meutter, E. Goormaghtigh, A. Dazzi, V. Raussens, Determination of secondary structure of proteins by nanoinfrared spectroscopy, Anal. Chem. 95 (2) (2023) 621–627.

[45] C. Guo, M. Chen, L. Wu, Y. Pei, C. Hu, Y. Zhang, J. Xu, Nanocomposites of Ag_3PO_4 and phosphorus-doped graphitic carbon nitride for ketamine removal, ACS Appl. Nano Mater. 2 (5) (2019) 2817–2829.
[46] Z. Zhou, Q. Shang, Y. Shen, L. Zhang, Y. Zhang, Y. Lv, Y. Li, S. Liu, Y. Zhang, Chemically modulated carbon nitride nanosheets for highly selective electrochemiluminescent detection of multiple metal-ions, Anal. Chem. 88 (11) (2016) 6004–6010.
[47] C. Cheng, Y. Huang, X. Tian, B. Zheng, Y. Li, H. Yuan, D. Xiao, S. Xie, M.M.F. Choi, Electrogenerated chemiluminescence behavior of graphite-like carbon nitride and its application in selective sensing Cu^{2+}, Anal. Chem. 84 (11) (2012) 4754–4759.
[48] L. Chen, D. Huang, S. Ren, T. Dong, Y. Chi, G. Chen, Preparation of graphite-like carbon nitride nanoflake film with strong fluorescent and electrochemiluminescent activity, Nanoscale 5 (1) (2013) 225–230.